ADVANCED MATERIALS
www.advmat.de

Crosslinked Remote-Doped Hole-Extracting Contacts Enhance Stability under Accelerated Lifetime Testing in Perovskite Solar Cells

*Jixian Xu, Oleksandr Voznyy, Riccardo Comin, Xiwen Gong, Grant Walters, Min Liu, Pongsakorn Kanjanaboos, Xinzheng Lan, and Edward H. Sargent**

Organometal halide perovskites, in particular lead halide perovskites ($APbX_3$, where A indicates methylammonium or formanidinium molecular cations and X indicates halides such as I, Br, and Cl or mixtures thereof), are attractive as solar energy harvesters in view of their solution-processed manufacturability and strong light absorption.[1–3] Perovskite photovoltaics have rapidly achieved impressive solar-to-electricity power conversion efficiencies, growing from 3.8% in 2009[4] to greater than 20% in 2014.[5] Advances have been made through the use of mesoporous scaffolds[6–8] and also of planar electrodes.[9–14]

In view of the high efficiencies demonstrated, the topics of hysteresis[15–19] and long-term stability[20–22] are of intense interest. Significant progress has been made in overcoming instabilities in the perovskite active material.[23,24]

Specifically, since hybrid halide perovskites have a highly ionic character, they can decompose under external stresses such as moisture, solvents and heating cycles, especially if not fully encapsulated.[1–3] The resultant ionic complexes are then highly reactive with transition metal oxides[25] (such as MoO_3) and metal contacts.[21,26] Materials engineering strategies, such as adding crosslinking among perovskite grains,[27] have been shown to enhance the stability of the active material, including in the presence of moisture.

Given these major strides in active layer engineering, there exists now the opportunity to improve contacts and interfaces to enable further progress in stability. When perovskite devices employ a top hole-extracting contact, the engineering of the HTL (hole transport layer) offers an opportunity to add protection to the perovskite that underlies it.[23,28–31] The HTL should desirably be robust to external stresses, such as high operating temperatures, and at the same time efficiently facilitate hole extraction and thus promote overall device performance. It should also be transparent to produce rear-metal-contact reflections and also to enable semi-transparent and multiabsorber devices.[32,33]

The organic HTL, widely used in many top-performing perovskite solar cells, spiro-MeOTAD (2,2′,7,7′-Tetrakis(*N*,*N*-di-p-methoxyphenylamine)-9,9′-spirobifluorene), requires the ionic dopant Li-TFSI (bis(trifluoromethane)sulfonimide lithium salt) with additive tBP (4-tert-butyl pyridine).[5–8,14,27,34–37] This additive has been found to evaporate at 85 °C,[31,38,39] limiting devices' thermal stability and also curtailing their capacity to withstand subsequent processing steps. Further, this doping mechanism, which involves interactions with oxygen, requires fine control.[39–42] The additive tBP and ionic dopant Li-TFSI have been found to interact with the ionic perovskite layer and contribute thereby to the undesired introduction of water into the active layer, thus contributing to perovskite device degradation.[30,31,42] Small pinholes in spiro-MeOTAD layers were recently identified[26,29,42] and found to facilitate the migration of iodine-containing compounds from the perovskite, leading to corrosion of the metal top contact. Finally, the sensitivity of spiro-MeOTAD to solvents imposes severe constraints on subsequent solution-phase processing steps atop the device.[32]

To go beyond reliance on sensitive Li-doped spiro-MeOTAD atop the perovskite, alternatives such as opaque carbon-based hole-extracting contacts,[28] hybrid carbon nanotube-polymers,[31] and inorganic CuSCN[43,44] have been investigated. These have shown improved device stability and chemical robustness. To date, however, the benefits of these alternatives have come with costs to performance: they have each quantitatively degraded solar cells' open-circuit-voltage, hysteresis, and fill factor. For example, the fill factors shown in these devices[28,31,44,45] are typically appreciably below the benchmark value (≈ 75%) achievable in the state-of-art devices employing doped spiro-MeOTAD.[5,6,27,34–37] These compromises to performance have been ascribed to poor band level alignment and inefficient egress of charges across the resultant interface.

We pursued a new HTL strategy with the goals of protecting the perovskite, achieving the needed free carrier density and work function without the use of chemical dopant additives, and ultimately achieving high-performance perovskite solar cells that would exhibit enhanced stability.

Our approach (**Figure 1**a) employed crosslinking of the polymer HTL on top of the perovskite in order to render the material insoluble and thermally stable. We achieved the needed deep work function and high hole free carrier density via a remote doping strategy.

J. Xu, Dr. O. Voznyy, Dr. R. Comin, X. Gong, G. Walters, Dr. M. Liu, Prof. P. Kanjanaboos, Dr. X. Lan, Prof. E. H. Sargent
Department of Electrical and Computer Engineering
University of Toronto
35 St George Street, Toronto, Ontario
M5S 1A4, Canada
E-mail: ted.sargent@utoronto.ca
Prof. P. Kanjanaboos
Department of Materials Science and Engineering
Mahidol University
272 Rama 6 Road, Bangkok 10400, Thailand

DOI: 10.1002/adma.201505630

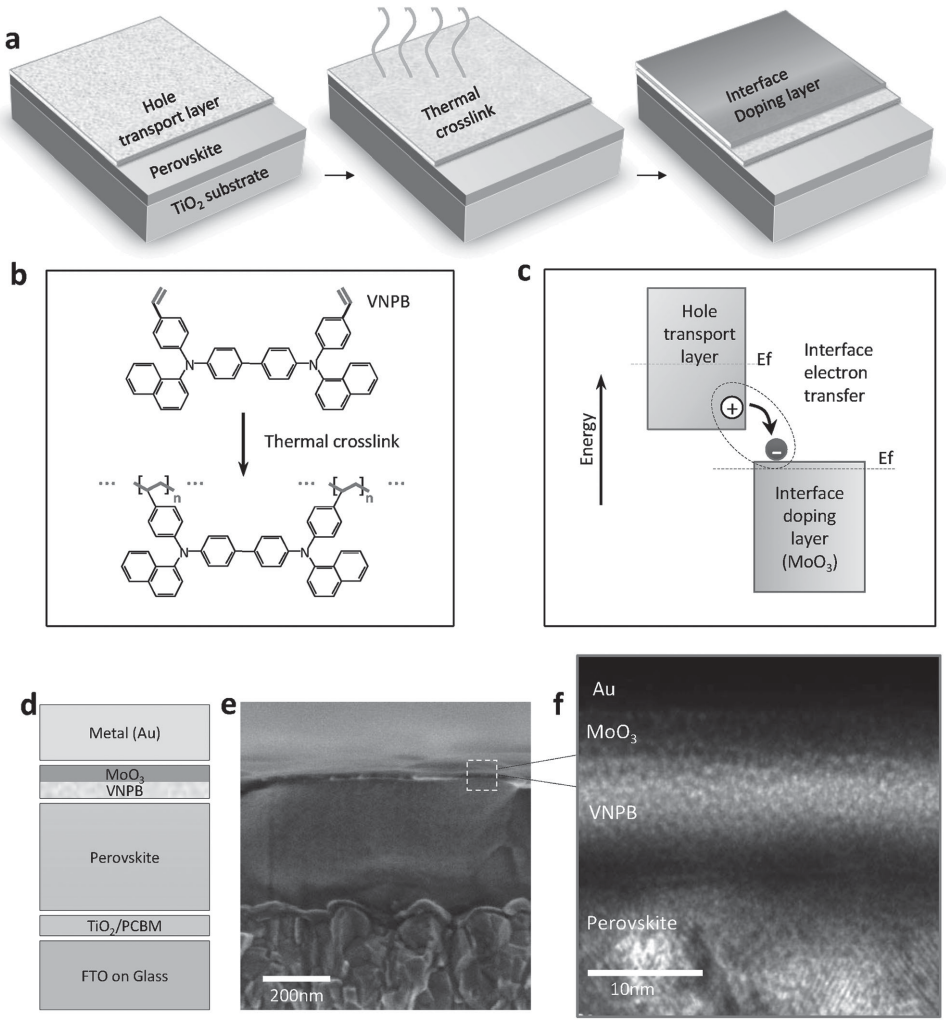

Figure 1. Hole extraction contact employing material crosslinking and interface doping. a) Two-step scheme to form the insoluble and thermally stable hole extraction contact. In the first step, the organic hole transport layer (HTL) is deposited and then thermally crosslinked; in the second step, an interface doping layer is simply deposited atop the HTL and doping is achieved via the interface charge transfer. b) Details of the thermal crosslinking process: double bonds in styrene groups in the hole transport layer (VNPB) are opened and then crosslinked via an addition reaction, thereby forming an insoluble, thermally stable film. c) Schematic of interface doping: ground-state electron transfer occurs from the hole transport layer, having low ionization-energy, to the interface with the high electron-affinity material, in this case transition metal oxide MoO_3, thereby enhancing the hole carrier density throughout the thin HTL. d) Device structure of the planar perovskite device using a VNPB-MoO_3 double-layer as the top hole extraction contact. e) The SEM cross-sectional image shows the full device covered by a dense hole extraction layer based on the VNPB-MoO_3 double-layer stack. f) High resolution TEM further resolves the fine interface of the VNPB-MoO_3 double-layer. VNPB and MoO_3 are confirmed to be in a dense and amorphous phase, forming a smooth interface with the underlying polycrystalline perovskite layer.

We focused the HTL work on arylamine derivatives, for these feature a HOMO (highest occupied molecular orbital) level similar to the ionization potential of the perovskite (5.4–5.5 eV). We first explored UV-crosslinkable arylamine derivatives (Figure S1, Supporting Information) based on cationic ring-opening polymerization of oxetane groups,[46–49] for these are known to be substantially inert when they are in intimate contact with underlying active materials. The crosslinking process employs a cationic photoinitiator to break the C—O bonds within each oxetane under UV radiation. It thereby constructs an insoluble network by forming a crosslinking C—O bond between different oxetanes.

Unfortunately, we witnessed much lower photovoltaic performance when compared to devices that used conventional Spiro-MeOTAD (Figure S1d, Supporting Information). We propose that known by-products[46,47] produced in situ by the cationic photoacid initiator used in the UV-crosslinking process degrade the electronic quality of the perovskite. We propose that the organometal halide perovskites are particularly sensitive and thus not immune to the cationic photoinitiator.

The observed in situ degradation motivated us to devise a perovskite-compatible crosslinking agent. We focused on nonionic polymerizable groups and found that by thermally inducing crosslinking between styrene groups,[50] we could form crosslinked films using the new arylamine derivative (N4,N4′-Di(naphthalen-1-yl)-N4,N4′-bis(4-vinylphenyl)biphenyl-4,4′-diamine), which we term VNPB.

Adv. Mater. 2016,
DOI: 10.1002/adma.201505630

When VNPB was deposited using spin-casting, it allowed us to form crosslinked films that did not evolve by-products that would degrade the underlying perovskite (Figure 1b). The needed crosslinking proceeds under mild thermal conditions and does not require the use of an initiator: instead, crosslinking is achieved by an addition reaction through the opening of the double bonds in styrene groups of adjacent VNPB units. Multiple styrene groups in each VNPB unit enable the formation of a 3D network with good coverage and strength.

Compared to the corresponding NPB film that lacks crosslinking groups, the VNPB film is insoluble and thermally stable, factors that enable the stacking of VNPB films via a layer-by-layer solution process (Figure S2, Supporting Information). Thermally induced polymerization of styrene groups has also recently been used to enhance an organic electrode interlayer that resides under the perovskite. Consistent with our findings, the crosslinked interlayer showed remarkable resistance to solvent-stress (perovskite-soluble polar solvents such as *N*,*N*-dimethylformamide (DMF)) and annealing-stress when perovskite was cast atop.[51]

The VNPB crosslinked layer is intrinsic, and thus incapable of efficient hole extraction from the perovskite. We sought to introduce free holes, and to do so without chemical doping used in Spiro-MeOTAD.[26,29–31,42] We pursued an interface remote doping strategy,[52] wherein we deposited a deep-work-function transition metal oxide layer atop the HTL (Figure 1a). The dense and chemically inert crosslinked VNPB would serve to keep physically separate, and thereby prevent chemical reactions among the perovskite and the metal oxide (MoO_3) layers.[25] The free hole density would be introduced into the otherwise-intrinsic HTL via ground-state electron transfer to the deep-workfunction metal oxide (MoO_3 in this work) at the organic–inorganic interface (Figure 1c).[53,54]

High resolution microscopy confirmed intimate contact between VNPB and MoO_3 (Figure 1d–f), a precondition for efficient interface electron-transfer. The VNPB-MoO_3 double-layer structure was also confirmed to be in a dense amorphous phase and thus suffered no issues of lattice mismatch with the polycrystalline perovskite. Ultraviolet photoelectron spectroscopy (UPS) studies confirmed that the HOMO level of the VNPB layer (−5.4 to −5.5 eV) is highly aligned with perovskite (Figure S3, Supporting Information), enabling a substantially barrierless hole extraction pathway.

The robust crosslinked hole transport layer (VNPB), coupled with an inorganic metal oxide layer (MoO_3) in a double-layer fashion, not only provides thermally stable and solvent-resistant protection for the perovskite, but also provides a stable and efficient doping process that leads to 16.5% solar power conversion efficiency (PCE) measured at steady state (Figure S4, Supporting Information).

In planar devices that employed the new contact strategy, we observed highly stable steady-state photovoltaic performance when the devices were operated at their maximum power point (**Figure 2**c, squares; see test details in the Experimental Section and Figure S4, Supporting Information). Their performance was equivalent to the benchmark devices that employed spiro-MeOTAD hole transport layers (Figure 2c, circles; Table S1, Supporting Information). External quantum efficiency (EQE) measurements were carried out and agreed with the measured current densities (Figure S5, Supporting Information).

We observed that the instantaneous *J*–*V*-curve provides a >80% fill factor with negligible hysteresis in planar devices (Figure 2b, Figure S4, Supporting Information). From a statistical analysis on a large sampling of devices that featured the new interfacial remote-doping hole-extraction contact (Table S1, Supporting Information), the average hysteresis was found to be low (2%), an improvement from our control devices that had used spiro-MeOTAD (6%). The low hysteresis agrees with the concept that the inert perovskite-crosslinked interface reduces chemical actions such as those seen with chemically doped Spiro-MeOTAD.[26,29–31,42] Here we quantify the hysteresis using Equation (1)

$$\text{Hysteresis} = \left(\frac{\text{Area}_{\text{forward}}}{\text{Area}_{\text{reverse}}} - 1\right) \times 100\% \quad (1)$$

where $\text{Area}_{\text{forward}}$ ($\text{Area}_{\text{reverse}}$) is the integrated area under the forward (reverse) scanning *J*–*V* curve. Low hysteresis correlates with stable steady-state output power. Devices with high hysteresis in *J*–*V* curves show decay of output current and power when operated at steady-state.[15,19,23] To avoid any overestimation of PCE arising from *J*–*V* hysteresis, we report the solar-to-electricity efficiency only using the steady-state power-to-power performance of devices operated at their maximum power point under constant AM1.5 solar illumination.

The high fill factor and low hysteresis indicate efficient charge extraction in the best-designed remote-doped devices. In contrast, the fill factor was seriously compromised in all undoped controls (Figure 2a,b, light gray curves). The steady-state performance of undoped controls is low, decays further during testing, and is accompanied by high hysteresis (Figure 2c). The same trend of device degradation occurs in both classes of undoped devices (spiro-MeOTAD devices without Li salt mixing; and crosslinked VNPB devices without a MoO_3 interface layer). This reconfirms the crucial role played by the MoO_3 layer in introducing across-the-interface remote doping in the crosslinked VNPB layer.

We sought mechanistic insights into the role of the interface doping. Specifically, we investigated the physical picture of interface doping at the VNPB-MoO_3 organic–inorganic heterojunction, and explored the design criteria for this new double-layer hole extraction structure.

UV–vis–IR spectroscopy provides one means to study electron transfer at the interface: when MoO_3 is deposited on top of a VNPB film, we observe a near-infrared absorption peak that we associate with the interface charge-transfer-complex.[55–58] This is in contrast with either individual VNPB or MoO_3 layers, which on their own are transparent in this wavelength region (Figure 2d). This sub-bandgap absorption feature has previously been associated in literature reports with the formation of intermediate states induced by charge-transfer-complexes at the donor-acceptor interface.[55–58] The attribution of this spectral feature to ground-state charge-transfer-complexes at the interface is further verified by photoluminescence (PL) quenching effects observed both in steady-state PL (Figure 2e, inset) and time-resolved PL measurements (Figure 2e). The PL tests reveal that the interfacial charge-transfer-complexes behave as quenching sites for excitons in

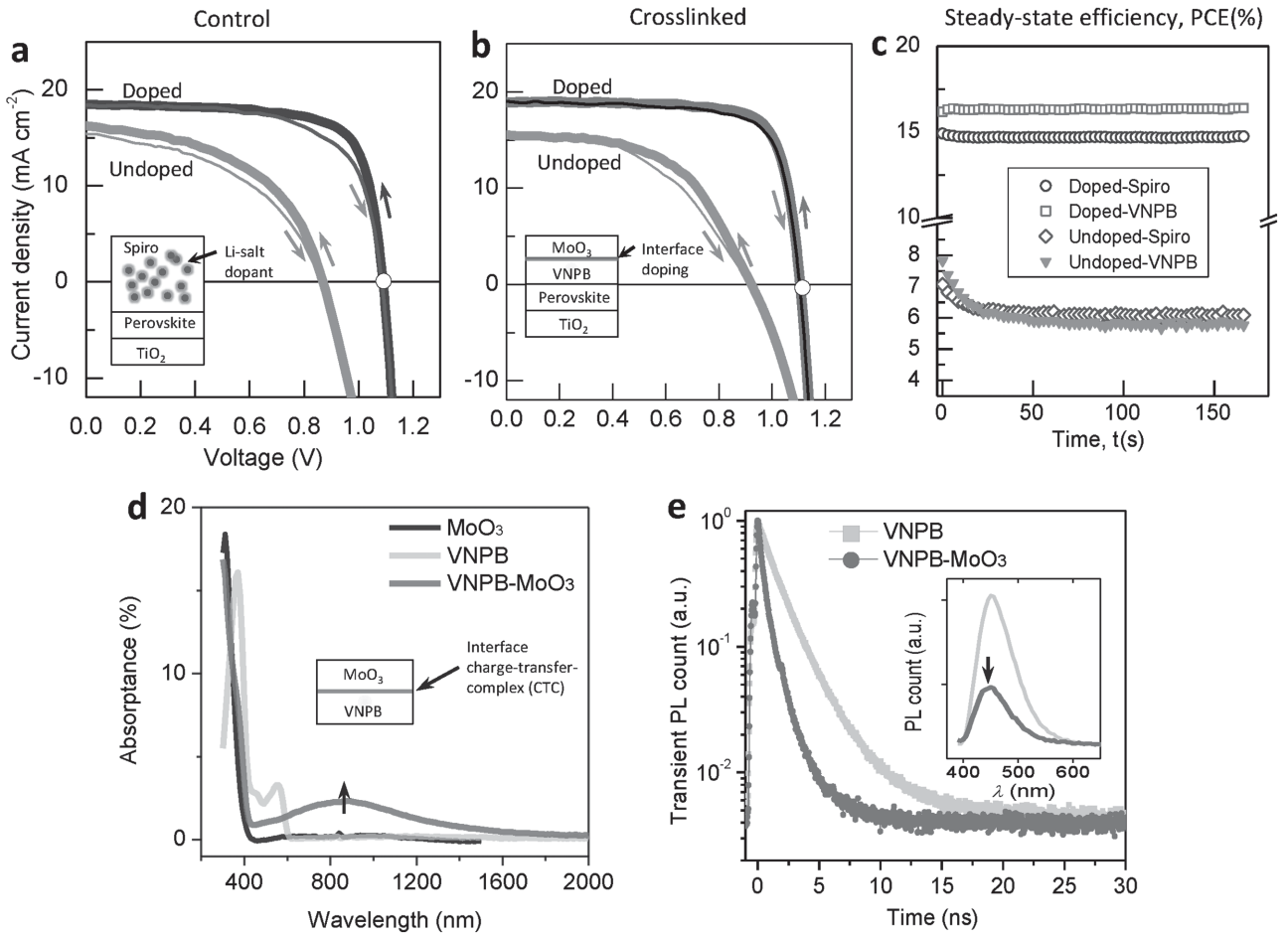

Figure 2. Improved photovoltaic performance with interface doping. a) The instantaneous *J–V* curve of control devices using doped Spiro-MeOTAD (dark gray) as the hole transport layer, compared with devices using undoped Spiro-MeOTAD (light gray). The undoped Spiro-MeOTAD leads to sharply reduced fill factor (FF) and performance. Arrows indicate the voltage scanning direction. The thicker curve is the forward scan starting from open circuit condition while the thin curve is the reverse scan starting from short circuit condition. The scanning rate is 0.2 V s^{-1}. The inset of (a) illustrates Spiro-MeOTAD doping by the use of Li salts throughout the film. b) The *J–V* curve of newly designed devices using the VNPB-MoO_3 interface doping hole-extraction contact (dark gray), compared with devices using VNPB alone (light gray). Without the interface doping, the FF and overall performance show a stark decline. In contrast, the device using interface doping shows an 80% FF with negligible hysteresis. The inset of (b) illustrates the doping at the interface of the VNPB-MoO_3 double-layer. c) Steady state power conversion efficiency (PCE) operated at the maximum power point of devices using interface doped VNPB (squares), doped Spiro-MeOTAD (circles), undoped VNPB (triangles) and undoped Spiro-MeOTAD (diamonds). The stable current output at maximum power point indicates no hysteresis, which is consistent with the observation in the test of instantaneous *J–V* shown in (b). The decay of steady-state PCE of undoped devices is typically associated with hysteresis in *J–V* curves. d) UV–visible–IR absorption spectroscopy of the VNPB-MoO_3 double-layer (dark gray) showing the signature (indicated by arrow) of the interface charge-transfer-complex (CTC) in the near-infrared absorption region, while MoO_3 (black) and VNPB individual layers (gray) exhibit no absorption features in the same wavelength region. Inset of (d) illustrates that the CTC resides at the interface when VNPB is covered by the interface doping layer MoO_3. e) The photoluminescence (PL) quenching effect in a VNPB-MoO_3 double-layer (dark gray) versus a VNPB single layer (light gray), induced by the interface charge-transfer-complex, is observed in transient and steady-state PL measurements (inset) of VNPB. The arrow indicates the VNPB PL peak (450 nm) where transient PL was measured.

VNPB films through polaron-exciton quenching.[59–61] Consistently, in spiro-MeOTAD, sub-bandgap absorption (Figure S6a, Supporting Information), PL quenching (Figure S6b, Supporting Information) and time-resolved-PL quenching (Figure S6c, Supporting Information) are observed only when spiro-MeOTAD is doped using the Li-salt. In VNPB-MoO_3, charge-transfer doping is accomplished at the interface alone, and therefore the absolute parasitic absorption is much less than that in bulk doped spiro-MeOTAD. These findings further agree with the picture of interface doping via ground-state electron-transfer at the VNPB-MoO_3 heterojunction depicted in Figure 1c.

Next we sought insights into the role of interface doping in devices. We made use of self-consistent optoelectronic device simulations[62] and looked particularly at the organic–inorganic interface of VNPB-MoO_3 in the steady state. The band-bending of VNPB and MoO_3 layers (**Figure 3**a,b) reconfirms the p-type doping of VNPB via interface electron-transfer. The theoretically predicted *J–V* behavior (Figure 3c) of solar devices with and without a MoO_3 interface doping layer are in excellent quantitative agreement with experimental results (Figure 2b). The simulations also predict that the interface doping layer will increase photovoltaic performance, most significantly through

Adv. Mater. **2016**,
DOI: 10.1002/adma.201505630

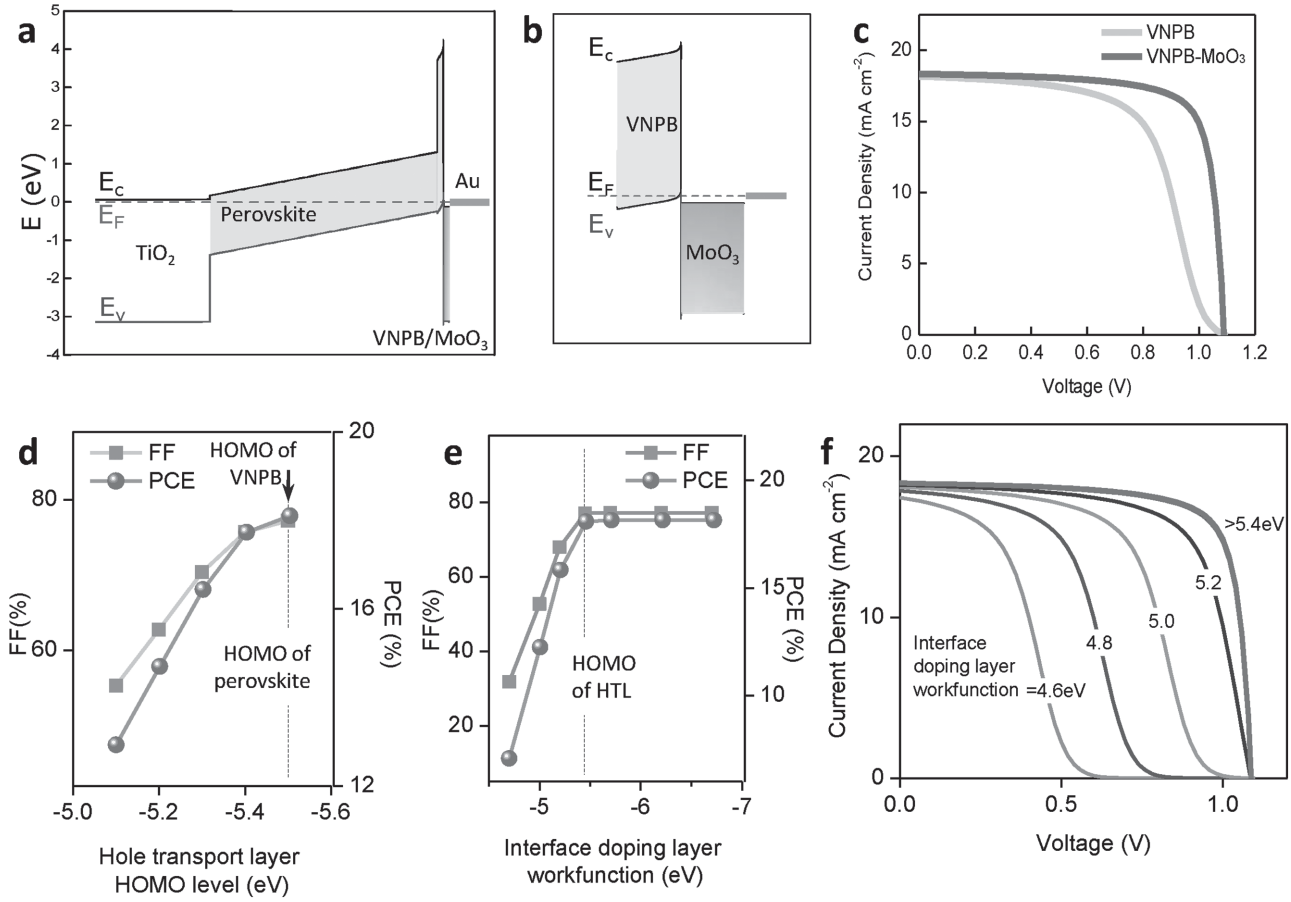

Figure 3. Electrical simulation of devices using interface doping. a) The equilibrium-state energy band diagram of devices using interface doping hole extraction contacts (VNPB-MoO_3). E_c (E_v) indicates the edge of the conduction (valence) band while E_f and dash line denote the Fermi level. b) Expanded view of the band alignment and band bending at the interface of the VNPB-MoO_3 double-layer stack. c) Performance comparison between devices with (dark gray) and without (light gray) interface doping layers. Without interface doping, the fill factor remarkably decreases, consistent with experimental observations (Figure 2b). d) Performance evolution when the HOMO level of the hole transport layer (HTL) changes. The fill factor increases when the HTL HOMO is well aligned with the HOMO of perovskite (dashed line). The arrow indicates that the HOMO level of crosslinked VNPB (5.46 ± 0.08 eV measured from UPS, Figure S3, Supporting Information) is highly aligned with the HOMO level of perovskite, and therefore is expected to result in the optimized performance when used as the HTL. e) Performance dependence on the workfunction of the interface doping layer. The fill factor is unaltered in a rather extended range (–5.4–7 eV), as long as the workfunction of the interface doping layer is deeper than the HOMO of the hole transport layer (dashed line). f) *J*–*V* curves corresponding to the performance evolution shown in (e) showing that the performance drop occurring when the workfunction of the interface doping layer becomes shallower than the HTL HOMO. The reported MoO_3 workfunction range resides in the optimal performance region.

the fill factor of devices. When we tune the HOMO level of the hole transport layer (Figure 3d), we observe linear control over the doping effect: fill factor increases when the HOMO of the hole transport layer moves toward the HOMO of the perovskite layer. VNPB satisfies this design rule very well, as confirmed by UPS measurements of the HOMO level (Figure S3, Supporting Information). With respect to the choice of work function, there exists a wide performance-insensitive region (Figure 3e,f), requiring only that the workfunction of the interface doping layer be deeper than the HOMO of the HTL (≈–5.4 eV). The hole extraction efficiency, associated with fill factor, declines sharply only when the workfunction of the doping layer is too shallow to accept electrons. Fortunately, the interface doping material MoO_3 resides, even when one accounts for the spread in reported workfunctions,[13,51–60] in the performance-insensitive region (–5.4 to –7 eV).

We then proceeded to assess the enhanced stability of the new devices under external stresses such as heating, moisture, and solvent. Devices with a remote-doped crosslinked top contact (VNPB-MoO_3) were first investigated under thermal stress. Most striking is the devices' retention of their superior performance (maintenance of at least 95% of initial performance) and low hysteresis behavior following fully 1 h of annealing at ≈100 °C (**Figure 4**b). Under the same stress, control devices with conventionally doped spiro-MeOTAD lost more than 30% of their performance irreversibly. This came principally through a severe degradation in fill factor and an increase in hysteretic behavior (Figure 4a). Consistently, the rectification, under dark conditions, of conventional devices also degraded irreversibly (Figure S7, Supporting Information). Similar trends as those for hysteresis degradation and performance decay in control devices were also observed in long-term steady-state

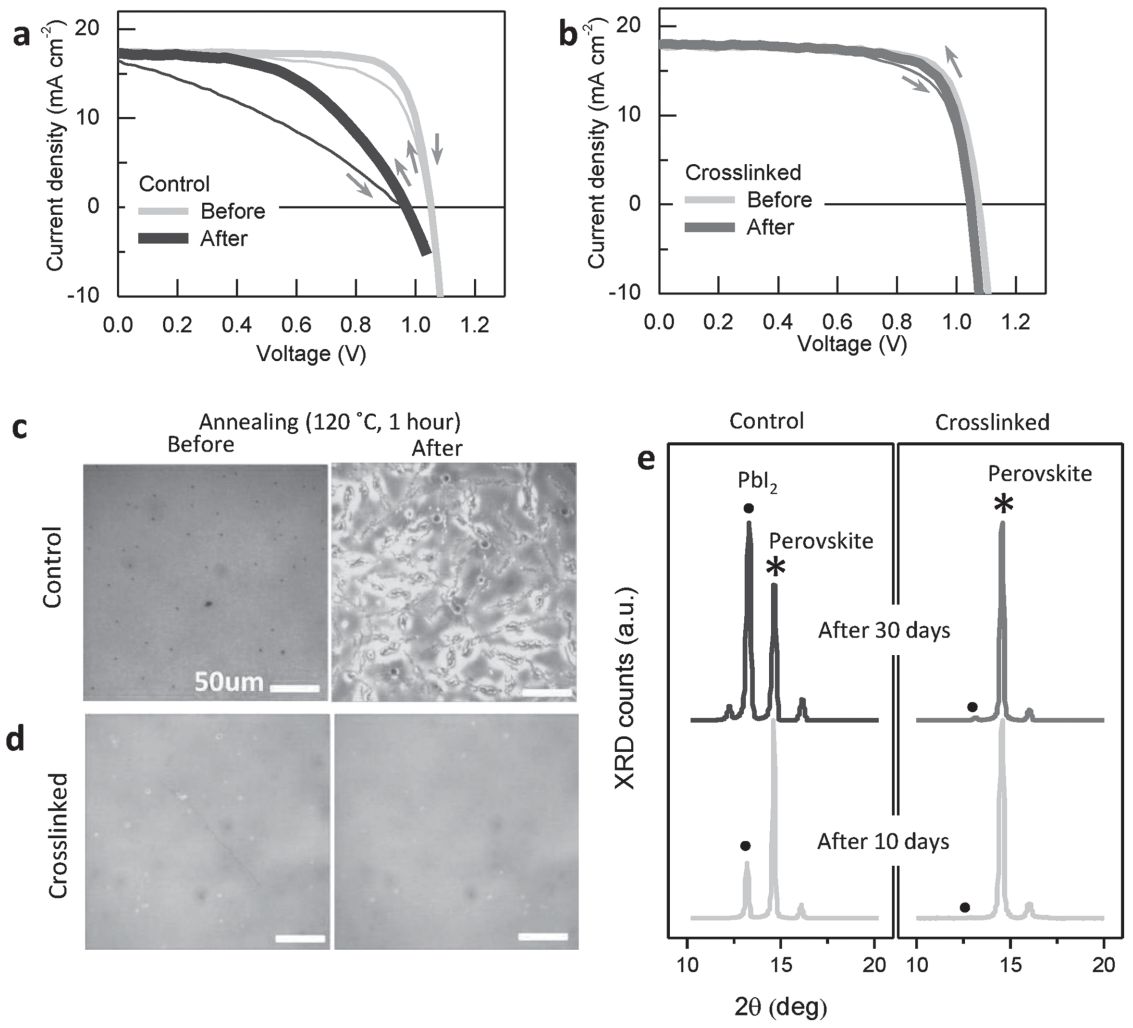

Figure 4. Evolution of performance, morphology, and material under external stress. a) The performance of devices using Spiro-MeOTAD as the hole-extraction contact tested at room temperature (light gray) and after a 110 °C burn-in test (dark gray) [In the burn-in test, devices are annealed at 110 °C for 1 h in an N_2 environment and tested after cooling down to room temperature]. b) The performance of devices using VNPB-MoO_3 tested at room temperature (light gray) and after 110 °C burn-in process (dark gray). c) Optical microscopy (reflection mode) of a doped Spiro-MeOTAD film before (left) and after burn-in (right). The annealed film shows chain-like structures, leading to the irreversible morphology degradation. d) The morphology of a VNPB-MoO_3 film before (left) and after burn-in (right). No visible morphology evolution can be observed. e) The evolution of perovskite content in the device active layer, tracked using the PbI_2 peak (•) and perovskite peak (*) in XRD measurements. Devices are tested after storage in air (70% RH, dark) for 10 and 30 d. PbI_2 peak of the perovskite film in a Spiro-MeOTAD device (left) emerges after 10 d (light gray) and dominates the perovksite peak after 30 d (dark gray), indicating severe decomposition of the perovskite phase. In contrast, the perovskite layer is well protected by the VNPB-MoO_3 film (right) and shows negligible PbI_2 signal even after 30 d (dark gray).

performance testing (Figure S10, Supporting Information). Just as in the undoped-spiro-MeOTAD devices (Figure 2a), the serious degradation in fill factor and the hysteresis indicates the loss of doping efficiency under such thermal stress. Additional direct evidence came from an optical microscopy study: we observed a new crystalline pattern in doped spiro-MeOTAD films (Figure 4c) following the thermal stress test. The irreversible morphology degradation is linked to the phase separation of dopant and spiro-MeOTAD host, a change that coincides with outgassing of the tBP additive at temperatures that exceed 85 °C.[31,38,39] In contrast, the morphology of the VNPB-MoO_3 double-layer is thermally stable (Figure 4d), attributed to the robustness of both the crosslinked material and the interface remote-doping mechanism.

We used X-ray diffraction (XRD) to explore the evolution of the perovskite active layer in devices placed under stress via the introduction of moisture (70% RH) combined with elevated temperatures. The degree of perovskite degradation was quantified by the ratio of PbI_2 peaks to perovskite peaks. In control devices with spiro-MeOTAD as the top contact, degradation is noticeable within 10 d and becomes significant after 30 d (Figure 4e, left). After 30 d the PbI_2 peak exceeds the perovskite signal, and the film is visibly yellow.

In contrast, following 30 d of moist heat, the perovskite in devices covered by the crosslinked layer did not change within measurement uncertainty (Figure 4e, right). This finding further confirms that the crosslinked hole transport layer, coupled with dense inorganic metal oxide in a double-layer

Adv. Mater. 2016,
DOI: 10.1002/adma.201505630

fashion, provides the perovskite with superior physical protection.

We also investigated the potential to adapt the new device structure in the direction of enabling multijunction cells. We measured the impact of subsequent solvent exposure (see details in Figure S8, Supporting Information), applying a polar solvent (methanol) often used in follow-on layer fabrication. The conventional spiro-MeOTAD device was much degraded as seen in its bandedge absorption change (Figure S9a, left, Supporting Information). When the same device is exposed to chlorobenzene, the sandwiched inorganic spiro-MeOTAD layer dissolves, producing irreversible loss of device structure and morphology (Figure S9b, upper, Supporting Information). We conclude that the conventional perovskite materials stack is vulnerable even when subjected to nominally orthogonal solvents.

In contrast, the device covered with a crosslinked HTL retains the active material and the device structure when exposed to both polar and nonpolar solvents (Figure S9a, right; Figure S9b, down side, Supporting Information). The enhanced resistance to heat, moisture, and follow-on solvent-based processing not only benefit the single cell, but also open avenues to fabricating multijunction devices atop the perovskite.

This work showcases a new methodology for hole extraction on top of planar perovskite solar cells. The crosslinked organic hole transport material, coupled with an inorganic metal oxide, provides an insoluble and inert physical protection layer, combined with high conductance for hole extraction. This enables device performance that is stable under longer duration and more intense external stresses than in many prior reports.

Experimental Section

Planar Solar Cell Fabrication: A thin TiO_2 compact layer was first formed on FTO (fluorine doped tin oxide) substrates using atomic layer deposition (≈10 nm, Cambridge Nanotech Savannah S100) using tetrakis-dimethyl-amido titanium and H_2O as precursors. A low-concentration $TiCl_4$ treatment was used for interfacial improvement. The substrates were soaked in $TiCl_4$ aqueous solution (120×10^{-3} M, 70 °C) for 30 min and then annealed at 500 °C for an additional 30 min. PCBM ([6,6]-phenyl-C61-butyric acid methyl ester, Nano-C, 99.5%) in chlorobenzene (≈20 mg ml^{-1}) was spin-cast on the TiO_2 substrates and then annealed at 70 °C for 10 min before the perovskite was then spin-cast on top. The planar perovskite layer was deposited using a modified method from a prior report.[19] Lead (II) acetate trihydrate (Sigma-Aldrich, 99.99%) should be dehydrated using acetic anhydride. Lead acetate ($Pb(C_2H_3O_2)_2$) and methylammonium iodide (MAI) (Dyesol, 99%+) were dissolved in DMF (Sigma-Aldrich, 99.9%) with the molar ratio 1:3 to form the perovskite precursor solution ($1–1.5 \times 10^{-3}$ M) and kept at 70 °C. Perovskite precursor is mixed with 20 µL PCBM in chlorobenzene (30 mg mL^{-1}) and deposited by spin-casting (3000–5000 rpm for 60 s) on preheated TiO_2-PCBM substrates in a nitrogen glovebox. The film was annealed at 75 °C for 5 min and then 100 °C for 20 min. For control devices using chemical doping, the hole transfer layer was deposited by spin-coating the mixture solution of Spiro-MeOTAD (Borun Chemical, 99%+), dopant Li-TFSI (Bis(trifluoromethane)sulfonimide lithium salt) and additive tBP (4-tert-butylpyridine) following a prior report.[6] For the interface doping devices, the hole transport layer VNPB (Lumtec, 95%+) in anhydrous toluene (3 mg mL^{-1}) was spin cast (3000–4000 rpm, 30 s) on perovskite film, followed by processing for the thermal crosslinking (120 °C for 25 min and 150 °C for 5 min). The interface doping layer was 10 nm MoO_3, evaporated under 10^{-7} Torr vacuum (Angstrom Engineering deposition system). After that, the samples were kept at 40 °C in the evaporation chamber for 10 min. The top metal contact was gold (50 nm) deposited through a shadow mask. Encapsulation was done using the UV cured epoxy (Ossila) in conjunction with a glass coverslip.

Steady-State Photovoltaic Performance and Hysteresis-Effect Characterization: The active area of devices was determined by an optical aperture (area 0.049 cm^2) placed before the device. The AM1.5 solar simulator (ScienceTech) was class A (<25% spectrum mismath) and the spectral mismatching factor was characterized using a Newport calibrated reference Si solar cell. The correction factor (CF) determined from the spectral mismatch factor was used to ensure accurate reporting of current density in our work (Equations (S1)–(S4), Supporting Information). The illumination intensity on devices was calibrated using a Melles–Griot power-meter to be 1 sun (100 mW cm^{-2}). The final accuracy of the solar-to-electricity measurements was estimated to be ±5%. Steady-state performance was measured using a Keithley 2400 SourceMeter. The standard testing process is as follows: first the steady-state open-circuit voltage $V_{OC}(t)$ was measured by fixing the current to zero; then short-circuit current $J_{SC}(t)$ was measured by setting the voltage to zero; third, the forward- and reverse-scanning instantaneous *J–V* curves were measured with a scanning rate of 0.2 V s^{-1} and the voltage of maximum power point (MPP) was determined. The *J–V* voltage scanning range was 1.1–1.2 times the steady-state open-circuit voltage. The hysteresis factor of *J–V* curves was quantified using Equation (1). Finally, the steady-state power conversion efficiency (PCE(*t*)) was measured by setting the bias at the maximum power point and tracking the output steady-state current for a certain duration. To avoid the overestimation due to the hysteresis effect, the figure of merit of photovoltaic performance was only determined by the steady-state efficiency. A standard steady-state testing of our representative device is shown in Figure S4 (Supporting Information). The long-term stability assessment is carried out by repeating the steady-state testing as shown in Figure S10 (Supporting Information).

Other Characterizations: UV–vis–IR absorption was measured using a PerkinElmer LAMBDA 950 Spectrophotometer. Steady-state and transient PL was carried out using the TCSPC function of a HORIBA FLuorolog-3 Spectrofluorometer, and following the method shown in literature to protect samples.[12] Samples were tested in a N_2 environment. EQE spectra were measured by aligning the cell to monochromatic illumination (a 400 W Xe lamp passing through a monochromator and appropriate cur-off filters). The active area was defined by the optical aperture before the cell, and the power was calibrated with UV–IR photodetectors (Newport 818-UV and Newport 838-IR). A solar simulator at 1 sun intensity provided the light bias. The monochromatic beam was chopped at 220 Hz. The response of the cell was measured with a preamplifier (Lakeshore) connected to a lock-in amplifier (Stanford Research 830) at short circuit conditions. XRD measurements were performed at room temperature with a Rigaku Miniflex 2-circle diffractometer operating in Bragg–Brentano scanning mode, with angular resolution of 0.01° and Cu-K radiation (0.154056 nm wavelength). UPS was carried out using He I (21.22 eV) photon lines from a discharge lamp.

Supporting Information

Supporting Information is available from the Wiley Online Library or from the author.

Acknowledgements

This publication is based in part on work supported by Award KUS-11-009-21, made by King Abdullah University of Science and Technology (KAUST), by the Ontario Research Fund - Research Excellence Program, and by the Natural Sciences and Engineering Research Council (NSERC) of Canada. The authors thank R. Wolowiec and D. Kopilovic for their

technical support. The authors thank Dr. Yongbiao Zhao and Yiying Li's help on UPS measurements.

Received: November 13, 2015
Revised: December 13, 2015
Published online:

[1] M. D. McGehee, *Nat. Mater.* **2014**, *13*, 845.
[2] M. Grätzel, *Nat. Mater.* **2014**, *13*, 838.
[3] M. A. Green, A. Ho-Baillie, H. J. Snaith, *Nat. Photonics* **2014**, *8*, 506.
[4] A. Kojima, K. Teshima, Y. Shirai, T. Miyasaka, *J. Am. Chem. Soc.* **2009**, *131*, 6050.
[5] W. S. Yang, J. H. Noh, N. J. Jeon, Y. C. Kim, S. Ryu, J. Seo, S. I. Seok, *Science* **2015**, *348*, 1234.
[6] J. Burschka, N. Pellet, S.-J. Moon, R. Humphry-Baker, P. Gao, M. K. Nazeeruddin, M. Grätzel, *Nature* **2013**, *499*, 316.
[7] M. M. Lee, J. Teuscher, T. Miyasaka, T. N. Murakami, H. J. Snaith, *Science* **2012**, *338*, 643.
[8] J. H. Heo, S. H. Im, J. H. Noh, T. N. Mandal, C.-S. Lim, J. A. Chang, Y. H. Lee, H. Kim, A. Sarkar, M. K. Nazeeruddin, M. Grätzel, S. I. Seok, *Nat. Photonics* **2013**, *7*, 486.
[9] P. Docampo, J. M. Ball, M. Darwich, G. E. Eperon, H. J. Snaith, *Nat. Commun.* **2013**, *4*, 3761.
[10] O. Malinkiewicz, A. Yella, Y. H. Lee, G. M. Espallargas, M. Graetzel, M. K. Nazeeruddin, H. J. Bolink, *Nat. Photonics* **2014**, *8*, 128.
[11] J. M. Ball, M. M. Lee, A. Hey, H. J. Snaith, *Energy Environ. Sci.* **2013**, *6*, 1739.
[12] S. D. Stranks, G. E. Eperon, G. Grancini, C. Menelaou, M. J. P. Alcocer, T. Leijtens, L. M. Herz, A. Petrozza, H. J. Snaith, *Science* **2013**, *342*, 341.
[13] Z.-K. Tan, R. S. Moghaddam, M. L. Lai, P. Docampo, R. Higler, F. Deschler, M. Price, A. Sadhanala, L. M. Pazos, D. Credgington, F. Hanusch, T. Bein, H. J. Snaith, R. H. Friend, *Nat. Nanotechnol.* **2014**, *9*, 687.
[14] M. Liu, M. B. Johnston, H. J. Snaith, *Nature* **2013**, *501*, 395.
[15] H. J. Snaith, A. Abate, J. M. Ball, G. E. Eperon, T. Leijtens, N. K. Noel, S. D. Stranks, J. T.-W. Wang, K. Wojciechowski, W. Zhang, *J. Phys. Chem. Lett.* **2014**, *5*, 1511.
[16] Z. Xiao, Y. Yuan, Y. Shao, Q. Wang, Q. Dong, C. Bi, P. Sharma, A. Gruverman, J. Huang, *Nat. Mater.* **2015**, *14*, 193.
[17] W. Tress, N. Marinova, T. Moehl, S. M. Zakeeruddin, M. K. Nazeeruddin, M. Grätzel, *Energy Environ. Sci.* **2015**, *8*, 995.
[18] Y. Shao, Z. Xiao, C. Bi, Y. Yuan, J. Huang, *Nat. Commun.* **2014**, *5*, 6784.
[19] J. Xu, A. Buin, A. H. Ip, W. Li, O. Voznyy, R. Comin, M. Yuan, S. Jeon, Z. Ning, J. J. McDowell, P. Kanjanaboos, J.-P. Sun, X. Lan, L. N. Quan, D. H. Kim, I. G. Hill, P. Maksymovych, E. H. Sargent, *Nat. Commun.* **2015**, *6*, 8081.
[20] J. You, L. Meng, T.-B. Song, T.-F. Guo, Y. Michael Yang, W.-H. Chang, Z. Hong, H. Chen, H. Zhou, Q. Chen, Y. Liu, N. De Marco, Y. Yang, *Nat. Nanotechnol.* **2015**, DOI 10.1038/nnano.2015.230.
[21] M. Kaltenbrunner, G. Adam, E. D. Głowacki, M. Drack, R. Schwödiauer, L. Leonat, D. H. Apaydin, H. Groiss, M. C. Scharber, M. S. White, N. S. Sariciftci, S. Bauer, *Nat. Mater.* **2015**, *14*, 1032.
[22] W. Chen, Y. Wu, Y. Yue, J. Liu, W. Zhang, X. Yang, H. Chen, E. Bi, I. Ashraful, M. Grätzel, L. Han, *Science* **2015**, *350*, 944.
[23] T. Leijtens, G. E. Eperon, N. K. Noel, S. N. Habisreutinger, A. Petrozza, H. J. Snaith, *Adv. Energy Mater.* **2015**, *5*, 1500963.
[24] J.-W. Lee, D.-H. Kim, H.-S. Kim, S.-W. Seo, S. M. Cho, N.-G. Park, *Adv. Energy Mater.* **2015**, *5*, 1501310.
[25] P. Liu, X. Liu, L. Lyu, H. Xie, H. Zhang, D. Niu, H. Huang, C. Bi, Z. Xiao, J. Huang, Y. Gao, *Appl. Phys. Lett.* **2015**, *106*, 193903.
[26] Y. Kato, L. K. Ono, M. V. Lee, S. Wang, S. R. Raga, Y. Qi, *Adv. Mater. Interfaces* **2015**, *2*, 1500195.
[27] X. Li, M. I. Dar, C. Yi, J. Luo, M. Tschumi, S. M. Zakeeruddin, M. K. Nazeeruddin, H. Han, M. Grätzel, *Nat. Chem.* **2015**, *7*, 703.
[28] A. Mei, X. Li, L. Liu, Z. Ku, T. Liu, Y. Rong, M. Xu, M. Hu, J. Chen, Y. Yang, M. Grätzel, H. Han, *Science* **2014**, *345*, 295.
[29] M.-C. Jung, S. R. Raga, L. K. Ono, Y. Qi, *Sci. Rep.* **2015**, *5*, 9863.
[30] W. Li, H. Dong, L. Wang, N. Li, X. Guo, J. Li, Y. Qiu, *J. Mater. Chem. A* **2014**, *2*, 13587.
[31] S. N. Habisreutinger, T. Leijtens, G. E. Eperon, S. D. Stranks, R. J. Nicholas, H. J. Snaith, *Nano Lett.* **2014**, *14*, 5561.
[32] J. P. Mailoa, C. D. Bailie, E. C. Johlin, E. T. Hoke, A. J. Akey, W. H. Nguyen, M. D. McGehee, T. Buonassisi, *Appl. Phys. Lett.* **2015**, *106*, 121105.
[33] L. Kranz, A. Abate, T. Feurer, F. Fu, E. Avancini, J. Löckinger, P. Reinhard, S. M. Zakeeruddin, M. Grätzel, S. Buecheler, A. N. Tiwari, *J. Phys. Chem. Lett.* **2015**, *6*, 2676.
[34] N. J. Jeon, J. H. Noh, W. S. Yang, Y. C. Kim, S. Ryu, J. Seo, S. I. Seok, *Nature* **2015**, *517*, 476.
[35] N. J. Jeon, J. H. Noh, Y. C. Kim, W. S. Yang, S. Ryu, S. I. Seok, *Nat. Mater.* **2014**, *13*, 897.
[36] J.-H. Im, I.-H. Jang, N. Pellet, M. Grätzel, N.-G. Park, *Nat. Nanotechnol.* **2014**, *9*, 927.
[37] H. Zhou, Q. Chen, G. Li, S. Luo, T. Song, H.-S. Duan, Z. Hong, J. You, Y. Liu, Y. Yang, *Science* **2014**, *345*, 542.
[38] C. D. Bailie, E. L. Unger, S. M. Zakeeruddin, M. Grätzel, M. D. McGehee, *Phys. Chem. Chem. Phys.* **2014**, *16*, 4864.
[39] A. Abate, T. Leijtens, S. Pathak, J. Teuscher, R. Avolio, M. E. Errico, J. Kirkpatrik, J. M. Ball, P. Docampo, I. McPherson, H. J. Snaith, *Phys. Chem. Chem. Phys.* **2013**, *15*, 2572.
[40] U. B. Cappel, T. Daeneke, U. Bach, *Nano Lett.* **2012**, *12*, 4925.
[41] W. H. Nguyen, C. D. Bailie, E. L. Unger, M. D. McGehee, *J. Am. Chem. Soc.* **2014**, *136*, 10996.
[42] Z. Hawash, L. K. Ono, S. R. Raga, M. V. Lee, Y. Qi, *Chem. Mater.* **2015**, *27*, 562.
[43] P. Pattanasattayavong, G. O. N. Ndjawa, K. Zhao, K. W. Chou, N. Yaacobi-Gross, B. C. O'Regan, A. Amassian, T. D. Anthopoulos, *Chem. Commun.* **2013**, *49*, 4154.
[44] S. Ito, S. Tanaka, H. Vahlman, H. Nishino, K. Manabe, P. Lund, *ChemPhysChem* **2014**, *15*, 1194.
[45] S. Ito, S. Tanaka, K. Manabe, H. Nishino, *J. Phys. Chem. C* **2014**, *118*, 16995.
[46] C. D. Müller, A. Falcou, N. Reckefuss, M. Rojahn, V. Wiederhirn, P. Rudati, H. Frohne, O. Nuyken, H. Becker, K. Meerholz, *Nature* **2003**, *421*, 829.
[47] D. C. Müller, T. Braig, H.-G. Nothofer, M. Arnoldi, M. Gross, U. Scherf, O. Nuyken, K. Meerholz, *ChemPhysChem* **2000**, *1*, 207.
[48] H.-J. Jhuo, P.-N. Yeh, S.-H. Liao, Y.-L. Li, S. Sharma, S.-A. Chen, *J. Mater. Chem. A* **2015**, *3*, 9291.
[49] Y. Deng, E. Peng, Y. Shao, Z. Xiao, Q. Dong, J. Huang, *Energy Environ. Sci.* **2015**, *8*, 1544.
[50] N. Hayashi, R. Nishio, S. Takada, Patent US20120080666 **2012**.
[51] T.-Y. Chiang, G.-L. Fan, J.-Y. Jeng, K.-C. Chen, P. Chen, T.-C. Wen, T.-F. Guo, K.-T. Wong, *ACS Appl. Mater. Interfaces* **2015**, *7*, 24973.
[52] J.-H. Lee, J.-J. Kim, *Phys. Status Solidi A* **2012**, *209*, 1399.
[53] M. Kröger, S. Hamwi, J. Meyer, T. Riedl, W. Kowalsky, A. Kahn, *Appl. Phys. Lett.* **2009**, *95*, 123301.
[54] J. Meyer, S. Hamwi, M. Kröger, W. Kowalsky, T. Riedl, A. Kahn, *Adv. Mater.* **2012**, *24*, 5408.
[55] X. Zhou, J. Blochwitz, M. Pfeiffer, A. Nollau, T. Fritz, K. Leo, *Adv. Funct. Mater.* **2001**, *11*, 310.

[56] D.-S. Leem, H.-D. Park, J.-W. Kang, J.-H. Lee, J. W. Kim, J.-J. Kim, *Appl. Phys. Lett.* **2007**, *91*, 011113.
[57] T. Matsushima, Y. Kinoshita, H. Murata, *Appl. Phys. Lett.* **2007**, *91*, 253504.
[58] Y. Zhao, J. Zhang, S. Liu, Y. Gao, X. Yang, K. S. Leck, A. P. Abiyasa, Y. Divayana, E. Mutlugun, S. T. Tan, Q. Xiong, H. V. Demir, X. W. Sun, *Org. Electron.* **2014**, *15*, 871.
[59] T.-W. Ng, M.-F. Lo, Q.-D. Yang, M.-K. Fung, C.-S. Lee, *Adv. Funct. Mater.* **2012**, *22*, 3035.
[60] S.-J. Yoo, J.-H. Chang, J.-H. Lee, C.-K. Moon, C.-I. Wu, J.-J. Kim, *Sci. Rep.* **2014**, *4*, 3902.
[61] T. Matsushima, G.-H. Jin, Y. Kanai, T. Yokota, S. Kitada, T. Kishi, H. Murata, *Org. Electron.* **2011**, *12*, 520.
[62] M. Burgelman, P. Nollet, S. Degrave, *Thin Solid Films* **2000**, *361–362*, 527.